RMetS
Royal Meteorological Society

The effects of initial vortex size on tropical cyclogenesis and intensification

Gerard Kilroy* and Roger K. Smith
Meteorological Institute, Ludwig Maximilians University of Munich, Germany

*Correspondence to: G. Kilroy, Meteorological Institute, Ludwig-Maximilians University of Munich, Theresienstr. 37, 80333 Munich, Germany. E-mail: gerard.kilroy@lmu.de

Three high-resolution numerical simulations are carried out to investigate the effects of initial vortex size on tropical cyclogenesis and intensification, starting with a relatively weak initial vortex with a maximum tangential wind speed of 5 m s^{-1}, but located at different radii. In all simulations, there is a progressive organization of convectively induced, cyclonic relative vorticity into a monopole structure. As the initial vortex size is increased, the organization occurs later. In addition, the size of the vorticity monopole, the sizes of the inner and outer core tangential wind circulations and the lifetime intensity of the vortex all become larger. An explanation for this behaviour is offered in terms of a boundary-layer control of the overturning circulation. The findings are consistent with those of previous studies that bypass the genesis stage and start with appreciably stronger initial vortices.

Key Words: tropical cyclone; hurricane; typhoon; spin-up; cyclogenesis; intensification; vortex size; initial size

Received 19 May 2017; Revised 21 July 2017; Accepted 25 July 2017; Published online in Wiley Online Library

1. Introduction

In a recent study, Kilroy *et al.* (2017a) presented the results of a series of idealized, high-resolution, cloud-resolving, numerical simulations of tropical cyclone genesis, starting from a weak, cloud-free, axisymmetric, warm-cored vortex in a quiescent environment using a thermodynamic sounding based on data from an observed pre-genesis event. It was shown that, during a gestation period on the order of two days, there is a progressive organization of convectively induced, cyclonic relative vertical vorticity into a monopole structure. This organization takes place at relatively low wind speeds and while there is only a small increase in the maximum azimuthally averaged wind speed. After the gestation period, the vortex intensifies rapidly, achieving hurricane strength within 12 h. In this article, we investigate the dependence of the genesis process in the same model on the initial vortex size.

Observations have shown that tropical cyclones have a wide range of sizes, as measured, for example, by the radius of near-surface gale force winds or the radius of the outermost closed isobar at the surface (Merrill, 1984; Weatherford and Gray, 1988; Liu and Chan, 1999; Kimball and Mulekar, 2004; Rudeva and Gulev, 2007; Yuan *et al.*, 2007; Chavas and Emanuel, 2010, Lu *et al.*, 2011, Chan and Chan, 2012). At one end of the size spectrum is the occurrence of so-called midget storms, in which even the extent of gale-force winds is no more than 100 km from the storm centre (for example, the radius of gales in Tropical Cyclone *Tracy* that devastated the Australian city of Darwin on Christmas Day in 1974 was a mere 50 km). At the other end of the spectrum is Typhoon Tip (1979), which had gales extending out to 1100 km radius (Merrill, 1984). Observations have also shown that there is little correlation between the storm size and its intensity as measured by the maximum near-surface wind speed or the minimum surface pressure (Merrill, 1984; Weatherford and Gray, 1988; Chavas and Emanuel, 2010).

There have been numerous theoretical attempts to account for the size differences between storms, including the size changes that may occur during the lifetime of an individual storm (DeMaria and Pickle, 1988; Xu and Wang, 2010; Smith *et al.*, 2011; Chan and Chan, 2014; Frisius, 2015; Kilroy *et al.*, 2016; Tsuji *et al.*, 2016). Some of these studies have pointed to a monotonic relationship between the final size of storms and the size of the initial disturbance from which they form, a finding that motivates the present study in part. A further motivation is the fact that, in our view, most of the explanations for size change proffered in the aforementioned studies do not quantify the effects of deep convection. A third motivation is to extend previous numerical modelling studies (e.g. Chan and Chan, 2014) to include the genesis process.

The basic processes controlling vortex size are most easily understood in the context of an inviscid axisymmetric vortex (Smith *et al.*, 2011). In this case, the most appropriate definition of outer size would be the radius of the outermost gale-force tangential wind component just above the frictional boundary layer, for example at an altitude of 1 km (Kilroy *et al.*, 2016, section 3b). A key principle for understanding size behaviour is the conservation of absolute angular momentum M, which is defined as $rv + \frac{1}{2}fr^2$, where r is the radius, v is the tangential velocity at that radius and f is twice the background angular velocity about the vortex axis (in the case of the atmosphere, the Coriolis parameter). For a nascent cyclonic vortex with its axis of rotation vertical, air parcels (or more strictly rings of air) undergoing radial displacements towards or away from the axis will approximately conserve their value of M. As a result, those moving radially inwards will spin faster, while those moving radially outwards will spin more slowly. For air parcels at a

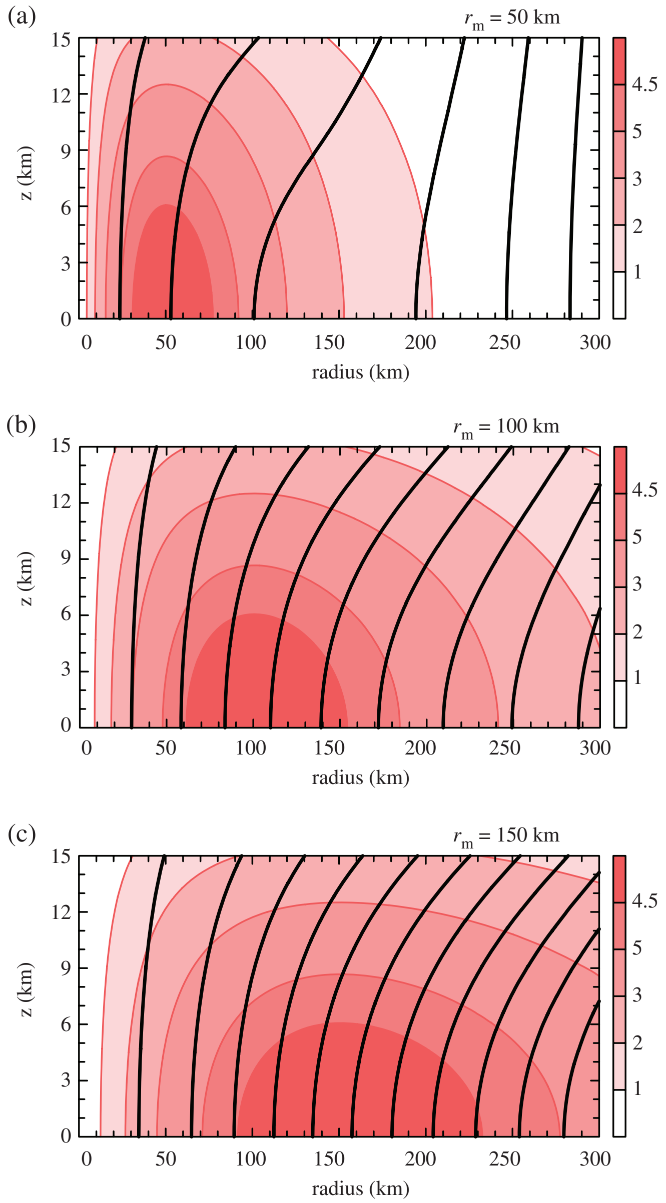

Figure 1. Vertical cross-section of the initial vortex structure in (a) E1, (b) E2 and (c) E3. Contours: V wind component as given by the shading in the label bar in units m s^{-1}. Contours of absolute angular momentum (black contours) in intervals of 1×10^6 m^2 s^{-1} starting from 0.5×10^6 m^2 s^{-1}. [Colour figure can be viewed at wileyonlinelibrary.com].

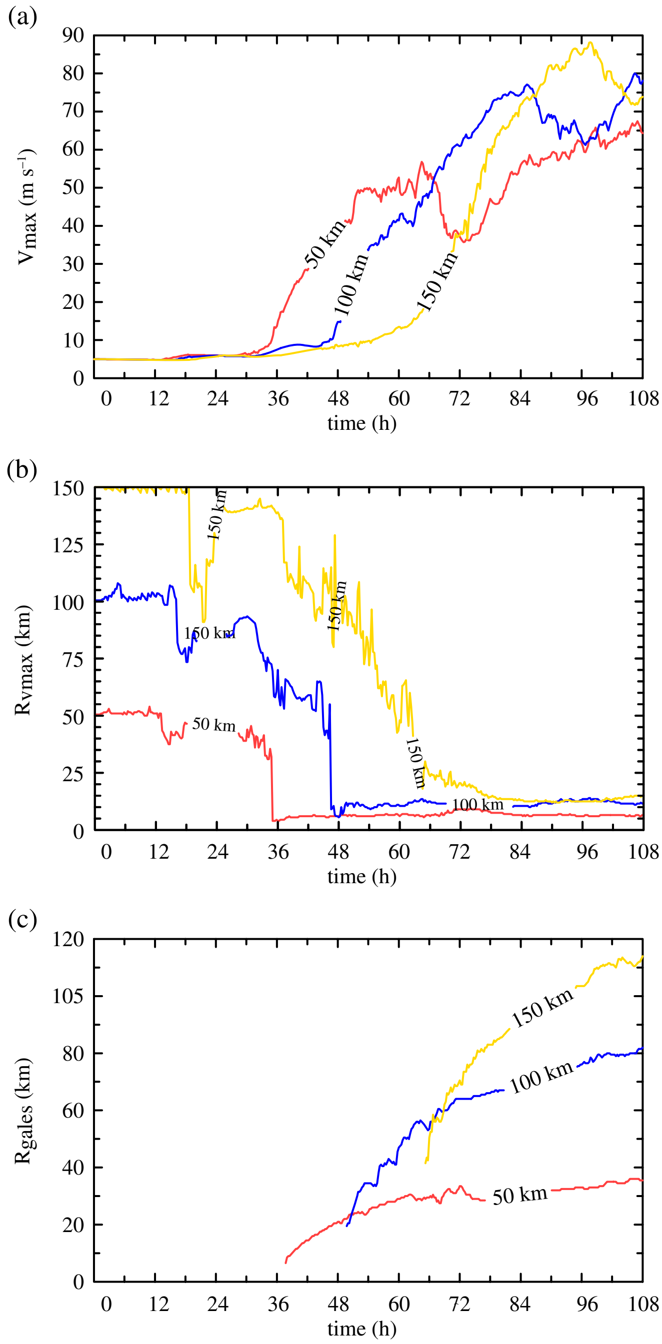

Figure 2. (a) Time series of maximum azimuthally averaged tangential wind speed (V_{max}). (b) Radius R_{vmax} at which V_{max} occurs. (c) Radius at which gale force winds occur (R_{gales}), where R_{gales} is calculated at a height of 1 km and corresponds to the radius of 17 m s^{-1} total wind outside the eyewall. [Colour figure can be viewed at wileyonlinelibrary.com].

particular location to be replaced by faster-moving ones, the inflow must occur in the presence of a positive radial gradient of M, i.e. where the nascent vortex is locally inertially stable. It follows that, for the vortex to amplify and thereby increase in size, some forcing mechanism is required to draw fluid parcels inwards towards the axis of rotation.

In the case of a tropical cyclone, the only conceivable mechanism capable of producing inflow above the frictional boundary layer is the entrainment induced by deep convection within the vortex circulation. Providing that the vortex is inertially stable (i.e. $\partial M^2 / \partial r > 0$) in the layer of convectively induced inflow, the tangential wind will continue to increase in this layer and, at least above the frictional boundary layer, the vortex will grow progressively larger in size.

From a geometrical perspective, the closer the convection is to the circulation centre, the more capable it would be of drawing air parcels in to small radii and thereby increasing the storm intensity, even though radial displacements of air parcels at small radii will be impeded more by the relatively high inertial stability there. The further deep convection extends from the vortex centre, the more capable it will be of producing inflow at large radii, where the weaker inertial stability will be less of an impediment to radial motion. Thus, the existence of outer convection must be conducive to increasing the storm outer size, as demonstrated by Xu and Wang (2010) and Tsuji *et al.* (2016).

The foregoing angular momentum principle does not apply in the boundary layer, because the frictional torque reduces the value of M, i.e. M is no longer materially conserved. However, at outer radii where the tangential wind in the boundary layer is subgradient, there should be a monotonic relationship between the radius of gale-force tangential wind near the surface and that just above the boundary layer. Indeed, calculations suggest a monotonic relationship between the radius of gales based on the tangential wind component at 1 km and that based on the near-surface total wind (see Kilroy *et al.*, 2017a, figure 2d).

The difficulties in trying to synthesize the quantitative effects of the foregoing processes (i.e. the effect of convection producing inflow in the lower troposphere giving rise to a radial import of M) arise because of the tight coupling between the deep

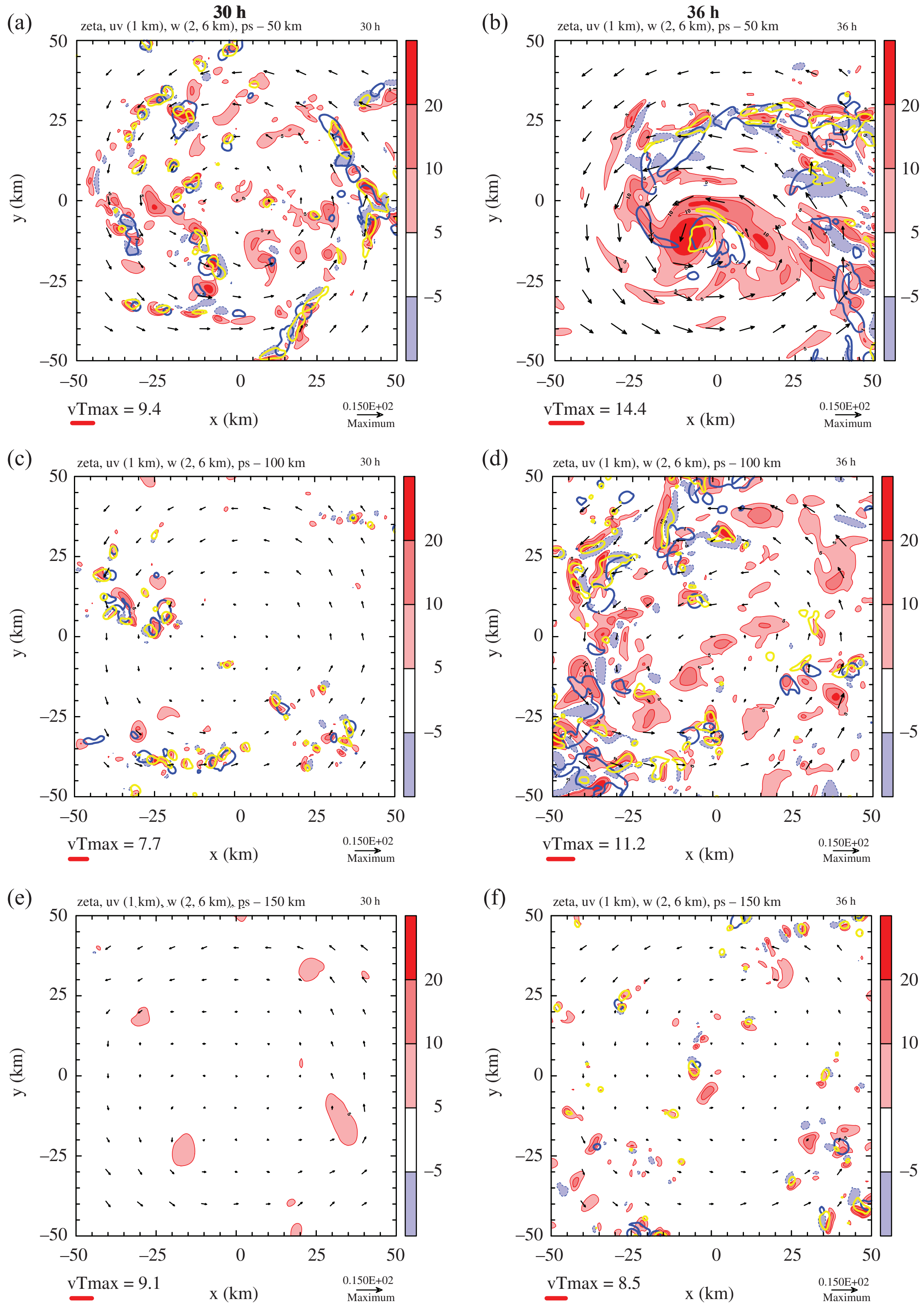

Figure 3. Horizontal cross-sections of relative vertical vorticity and wind vectors at various times for (a, b) E1, (c, d) E2 and (e, f) E3 at 30 and 36 h (additional times at 6 h intervals are shown in Figures 4 and 5). Also shown are contours of vertical velocity at heights of 2 km (blue) and 6 km (yellow) and black contours of surface pressure, contoured every 2 mb. Values for the shading of vertical vorticity are given in the colour bar, multiplied by 10^{-4}. The vertical velocity contour is 1 m s^{-1} for both heights. The wind vectors are scaled by the maximum reference vector (15 m s^{-1}) at the bottom right, while on the bottom left the maximum total wind speed in the domain plotted is given in m s^{-1}.

convection and the rotational field in which it is embedded, in part, through the dynamical and thermodynamical controls exerted by the frictional boundary layer (Kilroy *et al.*, 2016). Most purported explanations for the controls on vortex size focus largely on terms in the tangential momentum equation and, at best, give only a qualitative description of the deep convection that forces the inflow. We would argue that the rather complex conceptual diagrams presented by Xu and Wang (2010: see their figure 15) and Chan and Chan (2014: see their figure 18) obscure the overall simplicity of the individual process outlined above, without adequately detailing the coupling between the vortex evolution and deep convection. Echoing the discussion by Smith and Montgomery (2015), 'a minimum requirement of any acceptable theory for tropical cyclone intensification is that consideration be given to all dynamical and thermodynamic equations in a consistent manner'. This remark applies equally to

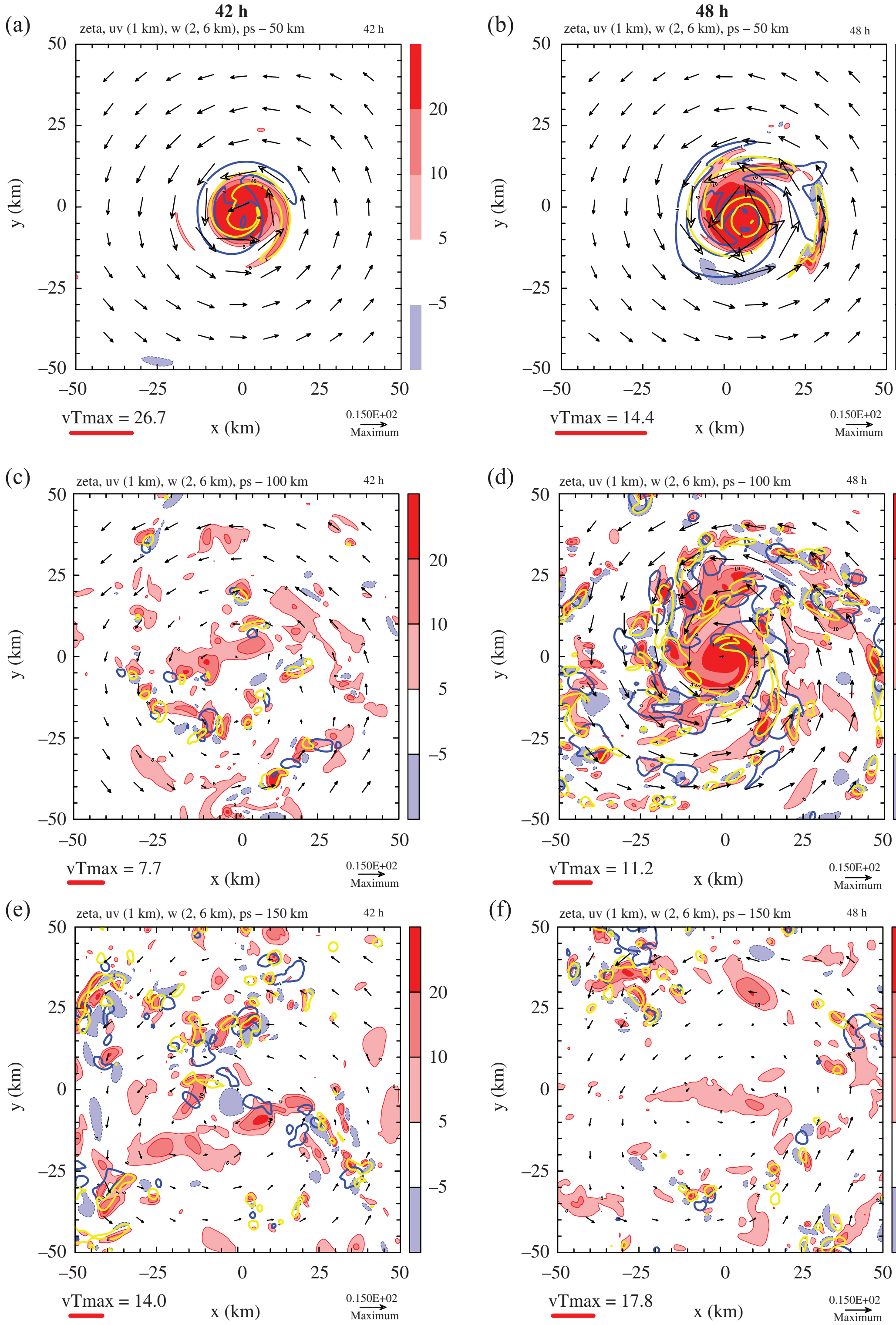

Figure 4. Legend as for Figure 3, but for 42 and 48 h.

an acceptable theory to explain tropical cyclone size changes. One cannot address the size problem solely by using the tangential momentum equation.

Clearly, the effectiveness of convection in producing inflow depends not only on its radial location, but also on its intensity and areal (including azimuthal) extent. It is therefore not surprising that cyclones in which deep convective rain bands extend relatively far from the circulation centre tend to have larger outer circulations compared with storms where deep convection is more confined, a feature demonstrated, for example, in the numerical simulations by Fudeyasu and Wang (2011) and in highly idealized simulations by Tsuji *et al.* (2016). Nevertheless, the question still remains as to why there are areal differences in the distribution of convection. Xu and Wang (2010) attribute the 'activity' of rain-band convection to the fact that surface enthalpy fluxes are larger in larger vortices, on account of the more extensive surface wind field, apparently overlooking the fact that the more extensive wind field above the boundary layer will also be accompanied by larger induced subsidence of dry air into the boundary layer, a consequence of boundary-layer dynamics. Moreover, they appear not to define precisely what they mean by an 'active rain band' or say how the degree of rain-band activity is quantified in relation to the surface enthalpy fluxes.

As is well known, convection occurs primarily where the convective inhibition (CIN) is sufficiently small or zero and the intensity of the convection, as characterized by the maximum vertical velocity or the mass flux it transports vertically, depends, *inter alia*, on the convective available potential energy (CAPE).

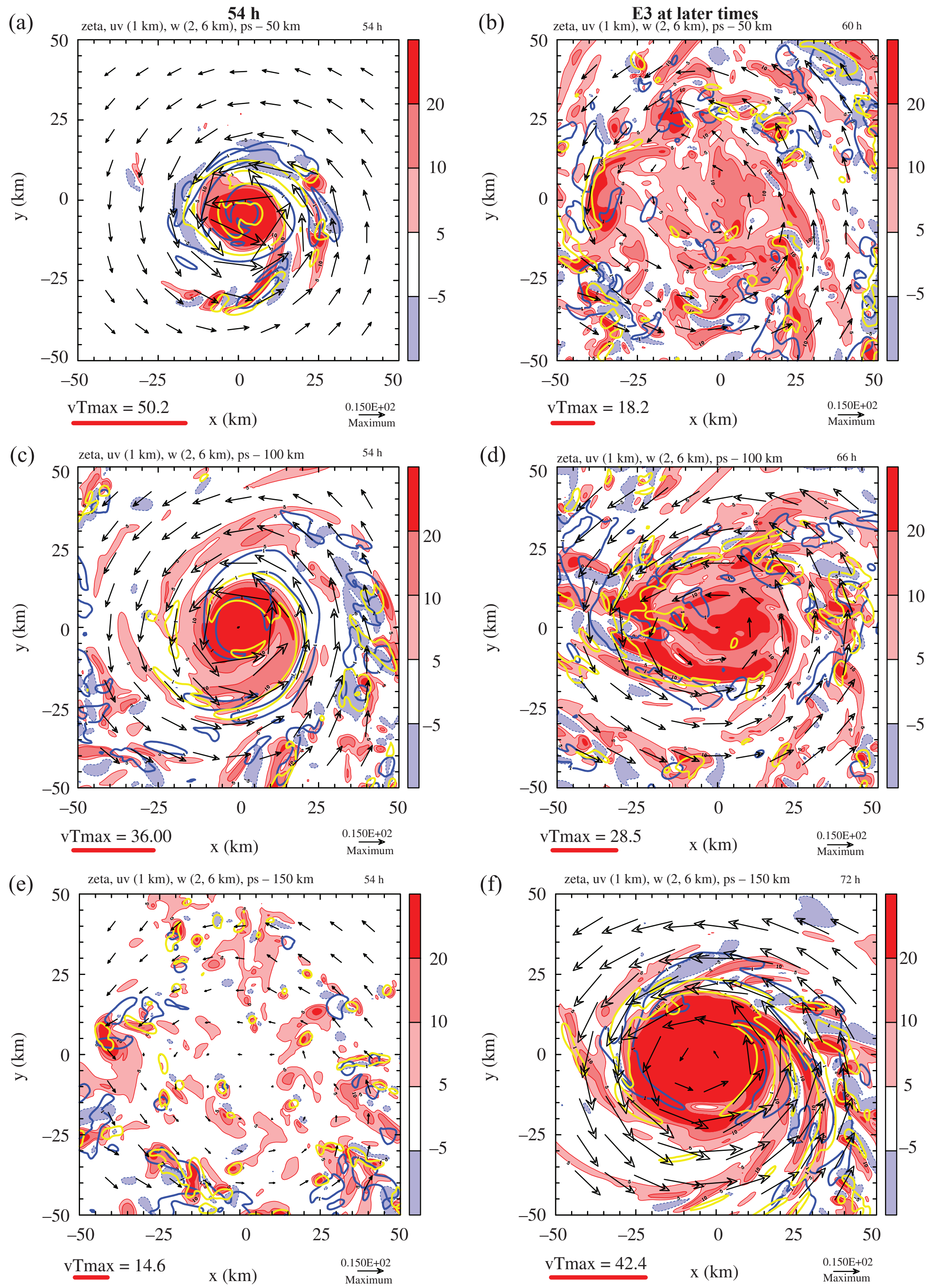

Figure 5. (a, c, e) Legend as for Figure 3, but for 54 h. (b, d, f) E3 at later times: (b) 60 h, (d) 66 h, and (f) 72 h.

We would suggest that robust explanations for controls on size require consideration of the controls on deep convection that drive the inflow to produce size changes. They require also a quantification of the convection in terms of, say, the diabatic heating rate and its spatial gradients and/or the convective mass flux. As noted above, important controls on deep convection are rooted in the dynamics and thermodynamics of the boundary layer.

One method to break into understanding the tight coupling between the vortex and boundary layer was proposed by Kilroy *et al.* (2016). These authors used a steady, axisymmetric, slab boundary-layer model driven by the diagnosed azimuthally averaged tangential wind field of their full numerical model to demonstrate the way in which the boundary layer controls the radial location and strength of the eyewall updraught, as well the expansion of the storm circulation with time.

The aim of the current study is to investigate the effects of initial vortex size on the genesis and intensification processes, with an emphasis on how the initial vortex size affects final inner- and outer-core sizes and intensity. Using high-resolution (500 m horizontal grid spacing) numerical simulations and a state-of-the-art three-dimensional model, we aim to provide a detailed view of the role of deep convection in controlling size.

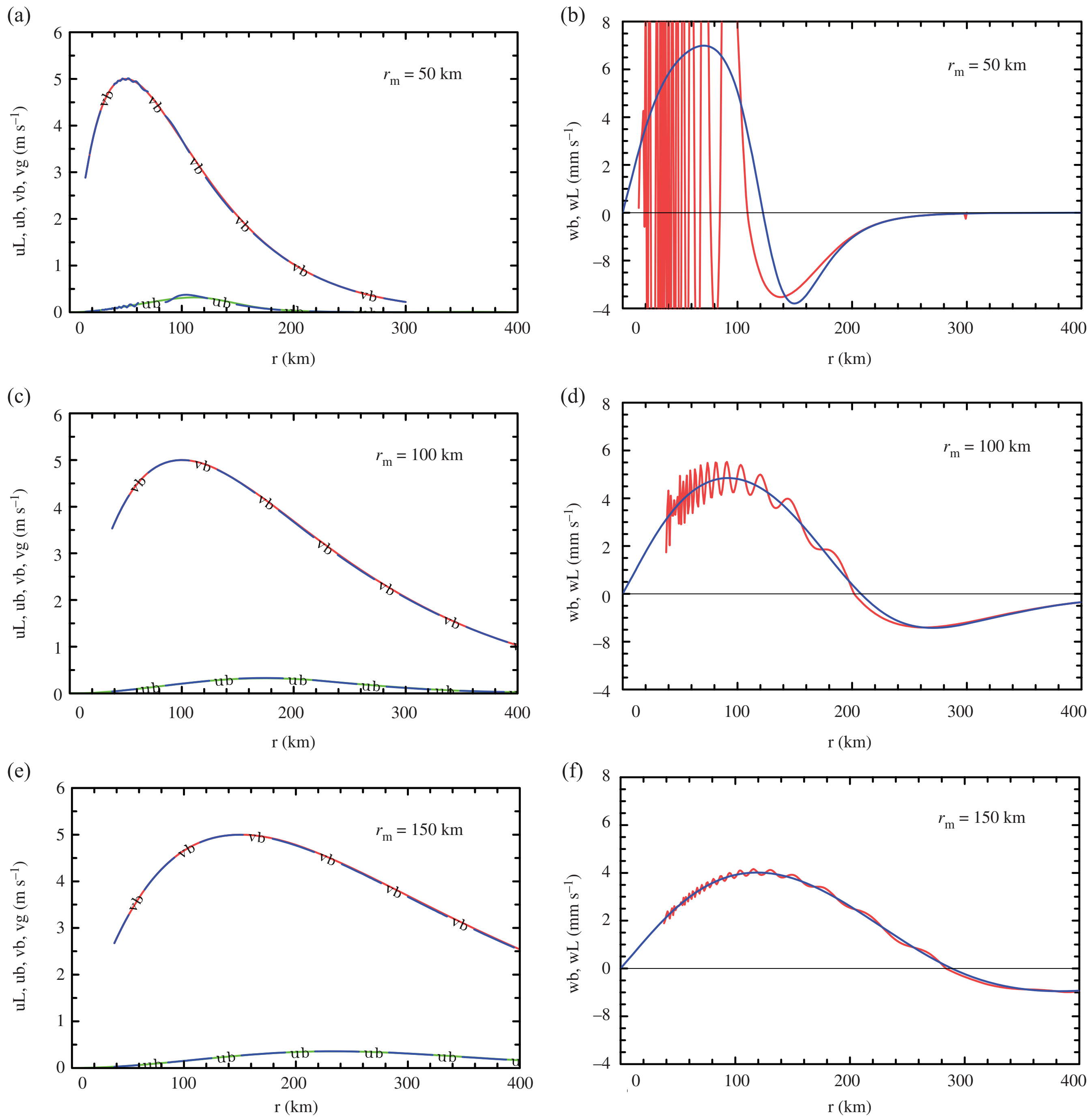

Figure 6. (a, c, e) Radial profiles of radial and tangential wind components, u_b and v_b, respectively, in the boundary layer (blue curves) for a fixed profile of gradient wind at the top of the boundary layer (the red line partially hidden), for (a) E1, (c) E2 and (e) E3. The green line (partially hidden) shows the radial inflow in the linear solution for the boundary layer. Panels (b, d, f) show the corresponding profiles of vertical velocity at the top of the boundary layer, calculated from the nonlinear solution (red curve) and the linear solution (blue curve) in (b) E1, (d) E2 and (f) E3. The calculations are based on the assumption of a constant boundary-layer depth of 1 km.

2. The numerical model and experimental design

The simulations described here have the same basic configuration as described in Kilroy *et al.* (2017a, 2017b). They relate to the evolution of a prescribed, initially weak, cloud-free, axisymmetric vortex in a quiescent environment on an f-plane and use the numerical model CM1 version 16, a non-hydrostatic and fully compressible cloud model (Bryan and Fritsch, 2002). In brief, the domain is $3000 \times 3000\,\mathrm{km}^2$ in size, with variable horizontal grid spacing reaching 10 km near the domain boundaries. The inner $300 \times 300\,\mathrm{km}^2$ has a uniform horizontal grid spacing of 500 m. The model is configured with 40 vertical levels extending to a height of 25 km. The vertical grid spacing expands gradually from 50 m near the surface to 1200 m at the top of the domain. The simulations are carried out on an f-plane with the Coriolis parameter $f = 2.53 \times 10^{-5}\,\mathrm{s}^{-1}$, corresponding to 10°N. Surface enthalpy fluxes are included in all simulations. The subgrid turbulence scheme used is the model option *iturb=3*, a parametrized turbulence scheme (Bryan and Rotunno, 2009). A simple warm-rain scheme is used, in which rain has a fixed fall speed of $7\,\mathrm{m\,s}^{-1}$. As in Kilroy *et al.* (2017a, 2017b), radiative effects are represented by adopting a simple Newtonian cooling approximation capped at 2 K per day, following Rotunno and Emanuel (1987).

The initial vortex is axisymmetric and warm-cored, with a maximum tangential wind speed of $5\,\mathrm{m\,s}^{-1}$ located at the surface. The initial temperature field is in thermal wind balance and is determined using the method described by Smith (2006). Figure 1 shows the structure of the initial vortex in the three experiments. The initial vortex is baroclinic and the tangential velocity profile is given by

$$v(r) = v_1 s \exp(-\alpha_1 s) + v_2 s \exp(-\alpha_2 s),$$

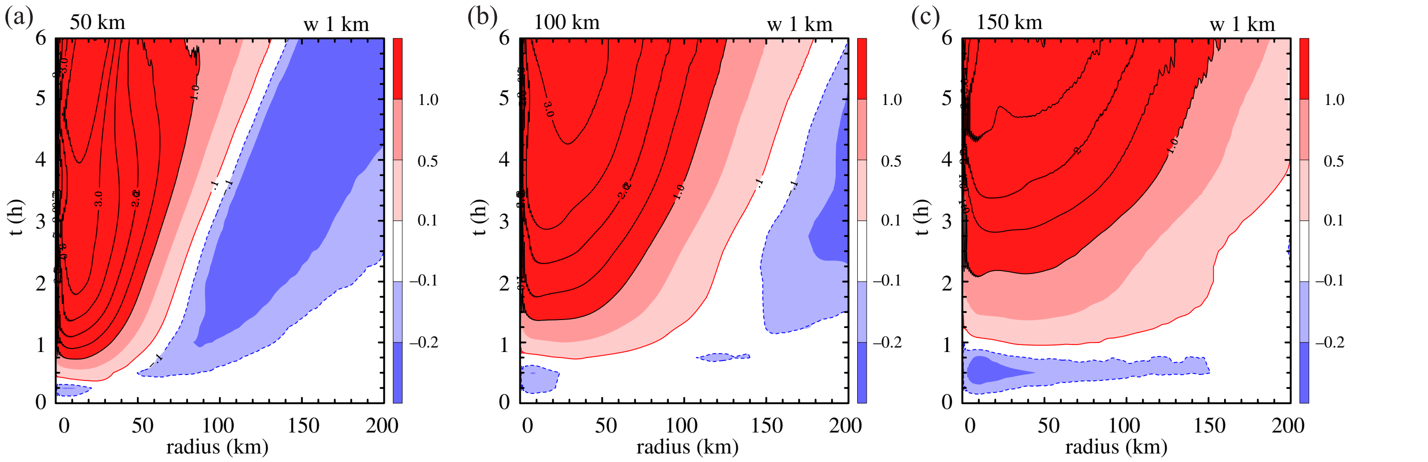

Figure 7. Azimuthally averaged Hovmöller plots of vertical velocity at a height of 1 km for (a) E1, (b) E2 and (c) E3 out to a radius of 200 km for the first 6 h of the simulation. Values for the shading are given in the colour bar, in units of mm s^{-1}. The black contours are every 1 mm s^{-1}. [Colour figure can be viewed at wileyonlinelibrary.com].

where $s = r/r_m$ and r_m, v_1, v_2, α_1 and α_2 are constants,* chosen to make $v = v_m = 5$ m s^{-1} at $r = r_m$. The initial tangential wind speed decreases sinusoidally with height, becoming zero at a height of 20 km. Three calculations are carried out, with the radius of the maximum tangential wind speed, r_m, located at 50, 100 and 150 km. We refer to these as E1, E2 and E3, respectively. Experiment E2 is the same as the control experiment in Kilroy *et al.* (2017a). Surfaces of absolute angular momentum (M-surfaces) are more tightly packed together as the initial vortex size increases, i.e. the inertial stability increases with increasing vortex size.

The reference sounding is the same as that used in Kilroy *et al.* (2017a, 2017b); see Kilroy *et al.* (2017a, figure 1). In brief, it is a mean of 39 dropsonde soundings obtained on 12 September 2010, during the Pre-Depression Investigation of Cloud Systems in the Tropics (PREDICT) field campaign for the tropical wave-pouch disturbance that eventually became Hurricane *Karl* late in the afternoon of 14 September (local time) (see Montgomery *et al.*, 2012; Smith and Montgomery, 2012 for details). This sounding has a CAPE† of 2028 J kg^{-1}, a CIN‡ of 47 J kg^{-1} and a total precipitable water (TPW) value of 61 kg m^{-2}. This sounding is moister (51.5 kg m^{-2} compared with 61 kg m^{-2}) than the Dunion moist tropical sounding (Dunion, 2011), although the Dunion sounding has a slightly larger CAPE (2104 J kg^{-1} compared with 2028 J kg^{-1}). For a more detailed comparison, see figure 1 and sections 2 and 3 of Kilroy *et al.* (2017a). The sea-surface temperature is 29 °C, typical of the Caribbean region at the time of *Karl*.

3. Vortex evolution

Figure 2 shows time series of various metrics that characterize the behaviour of the three experiments. These metrics include the azimuthally averaged maximum tangential wind speed (V_{max}), the radius at which V_{max} occurs (R_{vmax}) and the radius of gales (R_{gales}), defined as the outermost occurrence of azimuthally averaged gale force tangential wind at a height of 1 km (17 m s^{-1}).

The vortex centre used for azimuthal averaging is the location of the pressure minimum in a filtered surface pressure field as described by Kilroy *et al.* (2017a). The centre location is taken to be independent of height.

The V_{max} curves are almost identical for all three simulations until 33 h. Just after 33 h, the vortex in E1 begins a rapid intensification (RI) phase.§ As in Kilroy *et al.* (2017a), the vortex in E2 has an intensification begin time of about 45 h. In E3, the experiment that has the largest initial vortex, there is a more gradual intensification at first. The vortex in this experiment enters an RI phase at about 60 h. In all three experiments, there is a short decay following RI, with a restrengthening occurring afterwards (not shown). The lifetime maximum V_{max} increases with the size of the initial vortex, being 67.5 m s^{-1} in E1, 80.0 m s^{-1} in E2 and 88.2 m s^{-1} in E3.

In all three simulations, R_{vmax} begins to fluctuate from 12 h onwards following the development of deep convection. Nevertheless, there is a downward trend with time. In E1, R_{vmax} decreases abruptly to a value of about 5 km at 35 h and then remains below 10 km after RI. In E2, a similar sudden decrease in R_{vmax} occurs close to 47 h. In this simulation, R_{vmax} lies typically in the range between 9 and 13 km after RI. In E3, R_{vmax} undergoes a more gradual decrease, without a sudden drop as in E1 and E2. At 108 h it has a value of 15 km, although it increases to nearly 20 km over the next 16 h (not shown).

The first occurrence of R_{gales} in E1 is at a radius of 7 km near 38 h, while its value at 108 h is close to 35 km. In E2, R_{gales} occurs first at a radius of 20 km at about 50 h and has a value close to 80 km at 108 h. E3 has the largest vortex size in terms of the first location of R_{gales}, with a value of about 40 km near 66 h and a value of 115 km at 108 h. In all cases, R_{gales} is still increasing at 108 h.

In summary, as the size of the initial vortex is increased, the final vortex becomes stronger and has larger inner and outer core sizes, measured by R_{vmax} and R_{gales}, respectively. With a smaller initial vortex, genesis (and thus RI) occurs sooner. We will investigate the reasons for the more rapid development of a smaller initial vortex in the next sections.

4. Evolution of horizontal flow structure

In this section, we examine horizontal cross-sections of various fields in an inner core region 100 km × 100 km square centred on the vortex centre. These cross-sections illustrate the structure and evolution of the flow, including the locations of active deep convection prior to genesis. In Figures 3–5, we show a sequence

*The constants v_1 and α_1 are determined by the formulae $\alpha_1 = [1 - \mu\alpha_2 \exp(-\alpha_2)]/[1 - \mu \exp(-\alpha_2)]$ and $v_1 = v_m \exp(\alpha_1)[1 - \mu \exp(-\alpha_2)]$, where $\mu = v_2/v_m = 1.0$ and $\alpha_2 = 0.9$.

†We remind the reader that CAPE is a parcel quantity that typically has a strong negative vertical gradient in the lower troposphere. For this reason, the values cited herein are based on an average for air parcels lifted from the surface and at 100 m intervals above the surface to a height of 500 m. Since the calculation of CAPE is a nonlinear function of temperature and moisture, we prefer this method to one based on averaged values of temperature and mixing ratio through a surface-based layer of air with some arbitrarily prescribed depth.

‡Like CAPE, CIN is a quantity that also refers to an air parcel. Rather than computing an average up to 500 m as for CAPE, it seems physically more reasonable to examine the minimum value of CIN up to this level.

§RI is defined as an increase of V_{max} exceeding 15 m s^{-1} per day (Kaplan and DeMaria, 2003).

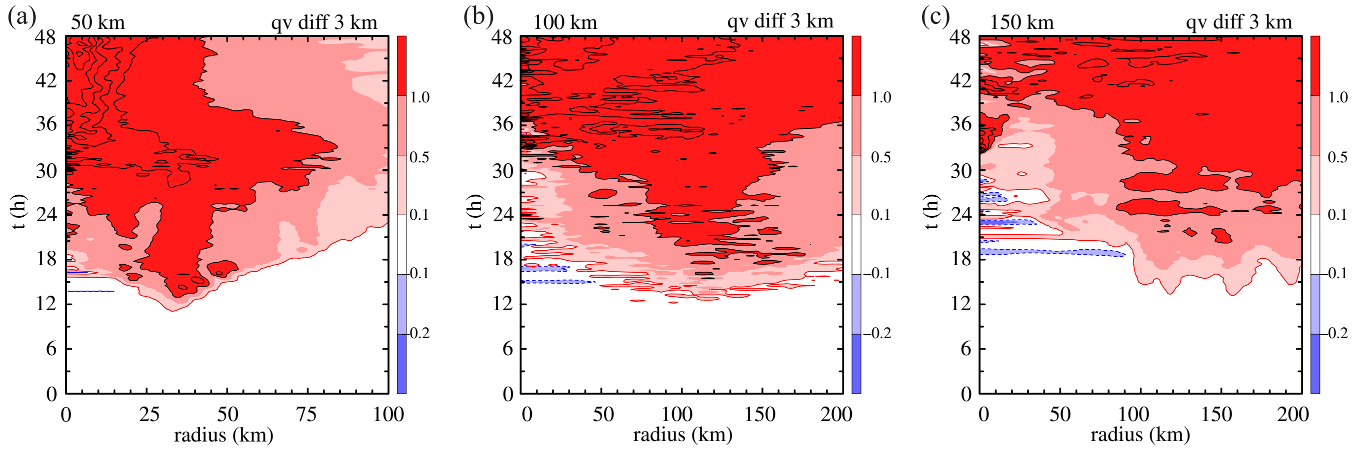

Figure 8. Azimuthally averaged Hovmöller plots of water-vapour mixing ratio difference from the initial profile at a height of 3 km for (a) E1, (b) E2 and (c) E3 out to a radius of 100 km for the first 48 h of the simulation. Values for the shading of water-vapour mixing ratio difference are given in the colour bar, in units of g kg^{-1}. The blue dashed contour is -0.1 g kg^{-1} and the solid black contours are every 1.0 g kg^{-1}. [Colour figure can be viewed at wileyonlinelibrary.com].

of horizontal cross-sections of vertical vorticity, wind vectors at a height of 1 km and surface pressure centred on the vortex centre at 6 h time intervals from 30 to 54 h for E1 and E2 and from 30 to 72 h for E3. Contours of vertical velocity equal to 1 m s^{-1} at heights of 2 and 6 km are superimposed to indicate the location of strong updraughts at these levels.

At 30 h, the inner core region in E1 is already convectively active (Figure 3(a)) and there are numerous patches of enhanced cyclonic vertical vorticity close to the vortex axis. This enhanced vorticity is generated by convective clouds that stretch and tilt the background vorticity. There is evidence of vorticity dipoles generated by tilting of background horizontal vorticity at, for example, (-30, 27.5 km), (40, 30 km) and (-5, -35 km). The vertical vorticity produced near the circulation centre tends to be mostly cyclonic on account of the lack of vertical wind shear (and thus a lack of horizontal vorticity) near the circulation centre (Kilroy and Smith, 2016). At this time, in E2, the same area is noticeably less convectively active (Figure 3(c)). Moreover, there are fewer patches of enhanced cyclonic vorticity present. In E3 there is no active convection at this time, although there are some remnants of enhanced vertical vorticity originating from prior deep convection (Figure 3(e)). As shown by Wissmeier and Smith (2011), the vorticity generated by deep convection generally outlives the convection itself.

The vortex in E1 begins to spin up around 33 h (Figure 2(a)) and by 36 h a clear monopole of strong vertical vorticity (values exceeding 2×10^{-3} s^{-1}) has emerged near the circulation centre (Figure 3(b)). There is some active convection near the monopole at this time and there is a spiral band of active deep convection emanating from the west side of the vortex core. This spiral band contains patches of both cyclonic and anticyclonic vertical vorticity. At this time in E2 (Figure 3(d)), there is a noticeable increase in the number of deep convective cells present in the domain shown and there are some patches of cyclonic vorticity located close to the circulation centre. In E3 there are now some active convective cells sparsely located over the domain shown (Figure 3(f)) and some of the patches of convectively induced cyclonic vorticity exceed 10×10^{-4} s^{-1} in magnitude.

In E1, a clearly defined 'midget' cyclonic vortex has developed by 42 h (Figure 4(a)). At this stage, V_{max} is close to 30 m s^{-1} and R_{vmax} is approximately 6 km (Figure 2). The vortex core is characterized by strong values of cyclonic vertical vorticity ($> 2 \times 10^{-3}$ s^{-1}) and there is still active convection over the vortex centre. In the following 6 h, the vortex in E1 has intensified further (Figure 4(b)), although its size remains small, with R_{gales} less than 30 km (Figure 2(c)).

At 42 h, there appears to be a reduction in convective activity in E2 from 6 h earlier (compare Figure 4(c) with Figure 3(d)), although this reduction is only temporary. The reduction in convective activity, which occurs in all three simulations, is linked to a flooding of the boundary layer with low values of equivalent potential temperature air following the convective activity (not shown). Over the next 6 h, deep convection engulfs the domain

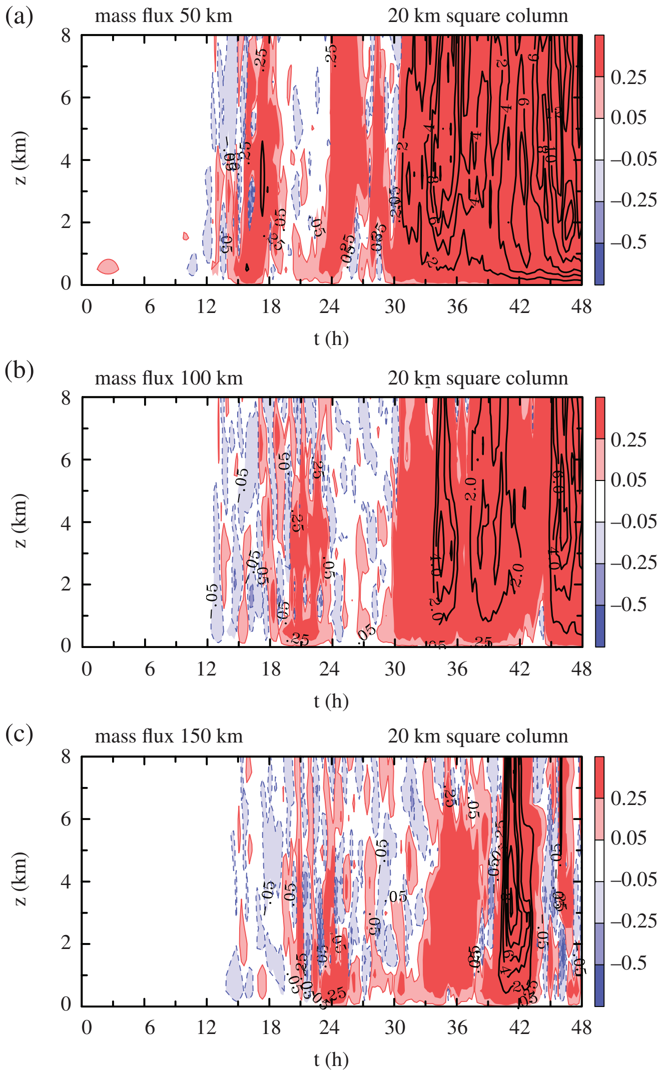

Figure 9. Time–height cross-sections of system-averaged mass flux within a 20 km × 20 km column, centred on the circulation centre in (a) E1, (b) E2 and (c) E3. Values for the shading of mass flux are given in the colour bar, in units of kg m^{-2} s^{-1} multiplied by 10 for plotting purposes. Thick black contours show values above 0.1 kg m^{-2} s^{-1}, contoured every 0.1 kg m^{-2} s^{-1}. [Colour figure can be viewed at wileyonlinelibrary.com].

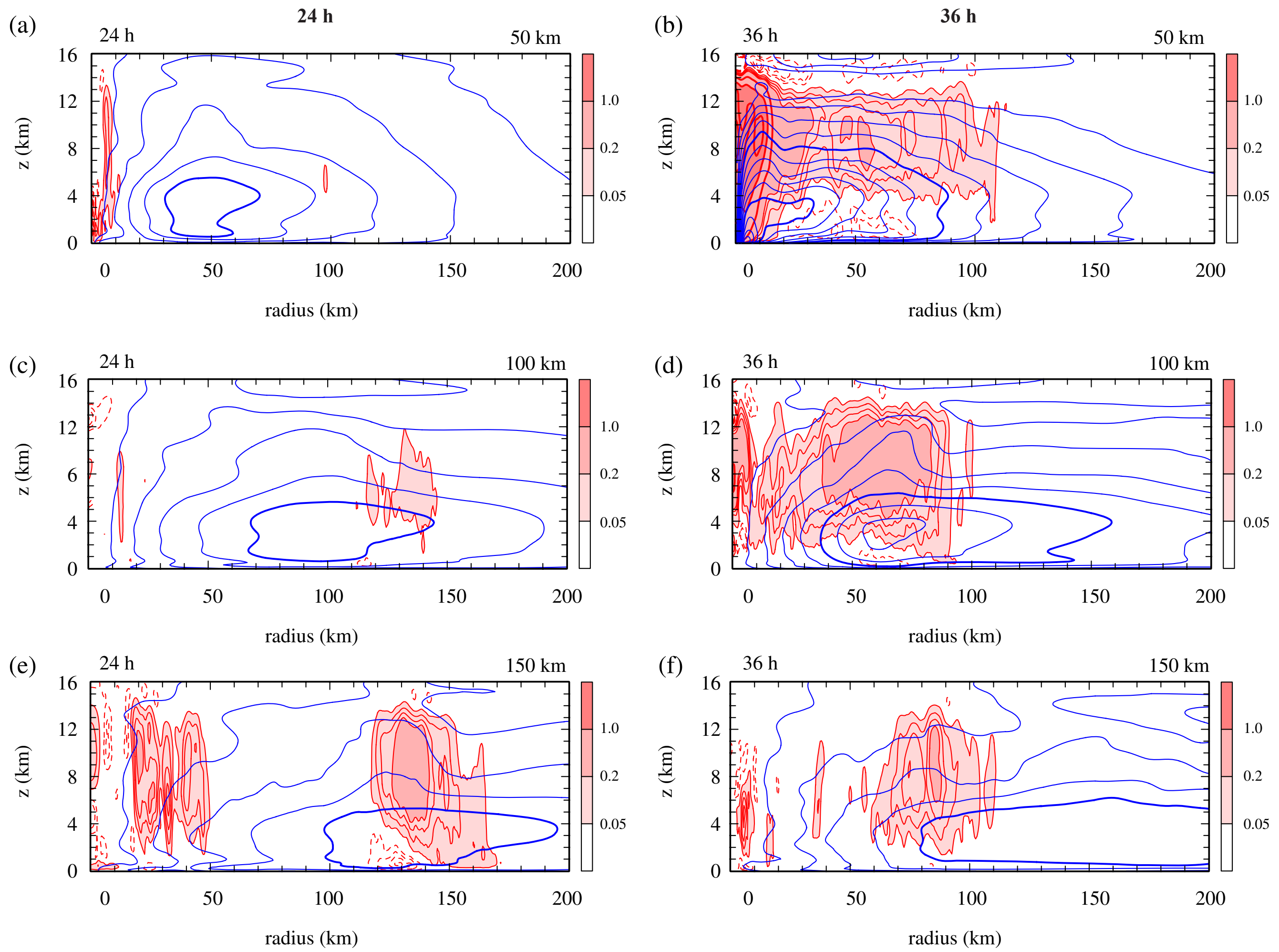

Figure 10. Vertical cross-sections of the azimuthally averaged, 3 h time-averaged tangential velocity component centred at (a, c, e) 24 h and (b, d, f) 36 h in (a, b) E1, (c, d) E2 and (e, f) E3. Superimposed are contours and shading of the averaged vertical velocity. Contour intervals are as follows. Tangential velocity: thin blue contours 1 m s^{-1} between 0 and 15 m s^{-1}, thick blue contours every 5 m s^{-1}. Vertical velocity: thin red contours every 0.05 m s^{-1} to 0.2 m s^{-1}, thick red contour interval 0.5 m s^{-1}, thin dashed red contours indicate subsidence at intervals of 0.02 m s^{-1}. Shading as indicated on the side bar. [Colour figure can be viewed at wileyonlinelibrary.com].

shown, with a strong ($> 2 \times 10^{-3}$ s^{-1}) core of cyclonic vorticity emerging near the circulation centre at 48 h. The vortex in E2 undergoes a period of RI beginning at 48 h. Repeated bouts of deep convective cells continually generate strong patches of cyclonic vertical vorticity close to the circulation centre and these vorticity anomalies migrate inwards, due largely to the collective effects of the inflow produced by the clouds themselves. The vortex subsequently spins up as cyclonic vorticity aggregates near the circulation centre. By 54 h, there is a clearly defined cyclonic core of vertical vorticity present near the circulation centre, with an eyewall-like feature evident in the vertical velocity field (Figure 5(c)).

Although there has been an increase in the number of convective cells in the domain shown at 42 h in E3 (Figure 4(e)), there has been essentially no increase in vortex strength in terms of $V_{\max}$ (Figure 2). By 54 h (Figure 5(e)), there are still few active cells near the circulation centre at this time. In order to cover the genesis and subsequent spin-up in E3, it is necessary to examine horizontal cross-sections at later times. These are shown in the right panels of Figure 5 at 6 h time intervals from 60 to 72 h.

By 60 h (Figure 5(b)), there has been a dramatic increase in convective activity as well as a major aggregation of cyclonic vorticity. Six hours later (Figure 5(d)), a partial eyewall of deep convection and a monopole of enhanced cyclonic vertical vorticity ($> 2 \times 10^{-3}$ s^{-1}) have formed. This monopole continues to strengthen and the surrounding eyewall feature becomes more coherent by 72 h. At this time (Figure 5(f)), the vortex has a $V_{\max}$ close to 40 m s^{-1}, while $R_{v\max}$ is close to 20 km.

5. The role of boundary-layer dynamics

For simplicity, we employ the simple, steady, slab boundary-layer model used by Kilroy *et al.* (2016) to help explain the differences in vortex evolution between the three experiments. The details of this model and the justification for its use are given in Smith *et al.* (2015). As in these previous studies, we assume that the boundary layer has a constant depth of 1000 m.

Figure 6 shows solutions for the radial, tangential and vertical velocity components, u_b, v_b and w_b, for a steady, slab boundary layer with the gradient wind profile used to initialize the present calculations (this profile has a maximum tangential wind speed of 5 m s^{-1} at a radius of 50 km for E1, 100 km for E2 and 150 km for E3). Kilroy *et al.* (2017b) found that a relatively weak initial vortex justified the use of a linear approximation in the boundary-layer model. This is because the tangential wind in the boundary layer is close to that above when the vortex is relatively weak (the vortex used in Kilroy *et al.* (2017b) is the same as that used in E2 here). Indeed, the linear solution gives a much smoother profile for w_b in all experiments (Figure 6, right panels). The nonlinear solution contains oscillations that are larger in amplitude when the initial vortex is narrower. As explained in Kilroy *et al.* (2017b), these oscillations are an unrealistic feature of the nonlinear slab boundary-layer model, but they are filtered out in the linear solution.

In all three experiments, the radial inflow in the boundary layer is relatively weak, with a maximum less than 0.5 m s^{-1} in magnitude. The larger the initial vortex, the further out the radial location of maximum inflow, the maximum being located

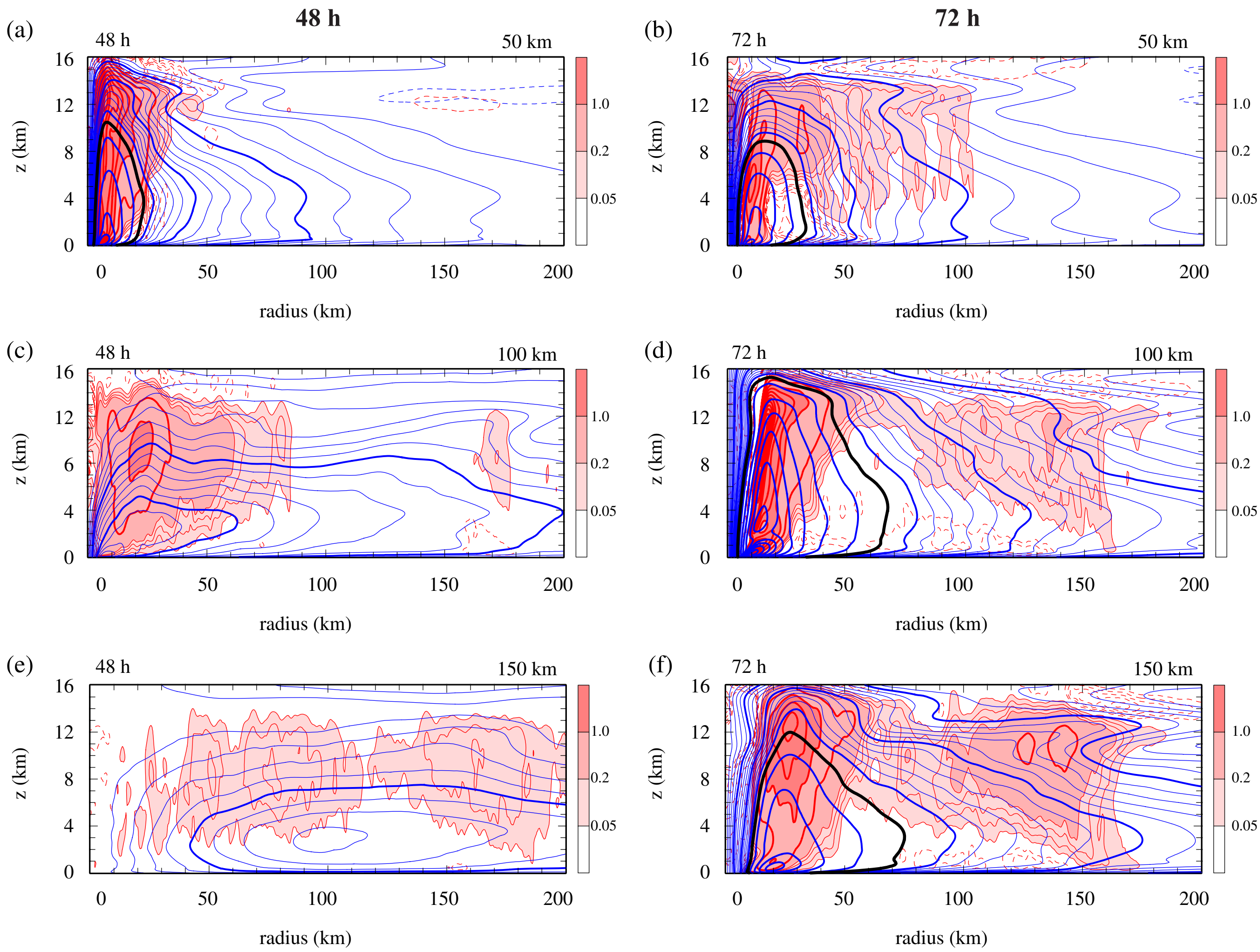

Figure 11. Legend as for Figure 10, but for (a, c, e) 48 h and (b, d, f) 72 h. An extra thick black contour represents gale-force winds (17 ms^{-1}). [Colour figure can be viewed at wileyonlinelibrary.com].

at radii of 100, 175 and 240 km in E1, E2 and E3, respectively. The boundary-layer inflow decreases in strength beyond these radii. The increasing magnitude of u_b with decreasing radius is accompanied at large radii by an increase in the rate of subsidence at the top of the boundary layer. In E1, w_b becomes positive at a radius of 120 km and reaches a peak of about 7 mm s^{-1} at a radius of 60 km. As the size of the initial vortex is increased, the flow out of the boundary layer is weaker, and the maximum upflow is located further radially outward.

These results are strong evidence that the initial vortex size determines the strength and location of the vertical velocity exiting the boundary layer. This upflow provides a suitable region for deep convection to develop and focus. Focusing the convection closer to the circulation centre at early times provides more favourable conditions for intensification to occur sooner, as discussed in the Introduction. Of course, the boundary layer in the model is not steady and requires time to become fully developed. For this reason, the foregoing results are suggestive rather than conclusive and further analysis is called for.

To illustrate the boundary-layer control at early times in the model itself, before deep convection occurs, in Figure 7 we show Hovmöller plots of the vertical velocity at a height of 1 km for the first 6 h of the simulation in the three experiments. As in the steady slab boundary-layer calculations, the upflow out of the boundary layer is stronger and more confined in radius as the initial vortex becomes narrower. Notwithstanding the fact that we are comparing a steady boundary layer with an evolving one, the vertical velocity profile from the numerical model corresponds broadly with that suggested by the slab boundary-layer model (compare with right panels of Figure 6). In particular, the location of the upflow and downflow regions is captured well by the slab boundary-layer model. These results suggest that the boundary layer controls the location of the upflow before any deep convection occurs and in this way determines the annulus in which the first bout of deep convection occurs.

Once deep convection develops, there is what might be described as a set of tightly coupled mechanisms controlling subsequent vortex evolution. The boundary-layer controls where the upflow out of the boundary layer occurs as well as the thermodynamic properties of the ascending air. The strength and thermodynamic properties of the upflow determine the spatial distribution of diabatic heating, which in turn, together with the inertial stability of the vortex, determines the strength and radial extent of the inflow above the boundary layer. This inflow leads to a spin-up of the tangential wind above the boundary layer and these strengthening winds bring about changes in the boundary-layer flow as a result of boundary-layer dynamics (Kilroy *et al.*, 2016). These mechanisms help us to interpret the differences in evolution of the azimuthally averaged flow fields in the three experiments discussed in section 6.

The moistening effects of the early focusing of convection close to the circulation centre for a smaller initial vortex are seen in Hovmöller plots of the difference (Δq) in azimuthally averaged water-vapour mixing ratio from its initial value at a height of 3 km (Figure 8). In E1, there is a strong moistening at a radius of about 35 km just after 12 h. By 24 h, the strong moistening has migrated inwards to the circulation centre. The vortex in E1 spins up about 12 h later (Figure 2(a)). The initial moistening in E2 occurs further out, at a radius of about 57.5 km. It takes about 12 h longer than in E1 for strong moistening to reach the vortex axis, i.e. at 36 h. By 48 h, the vortex in E2 has begun its RI phase. In E3, the initial moistening occurs at multiple locations (at radii

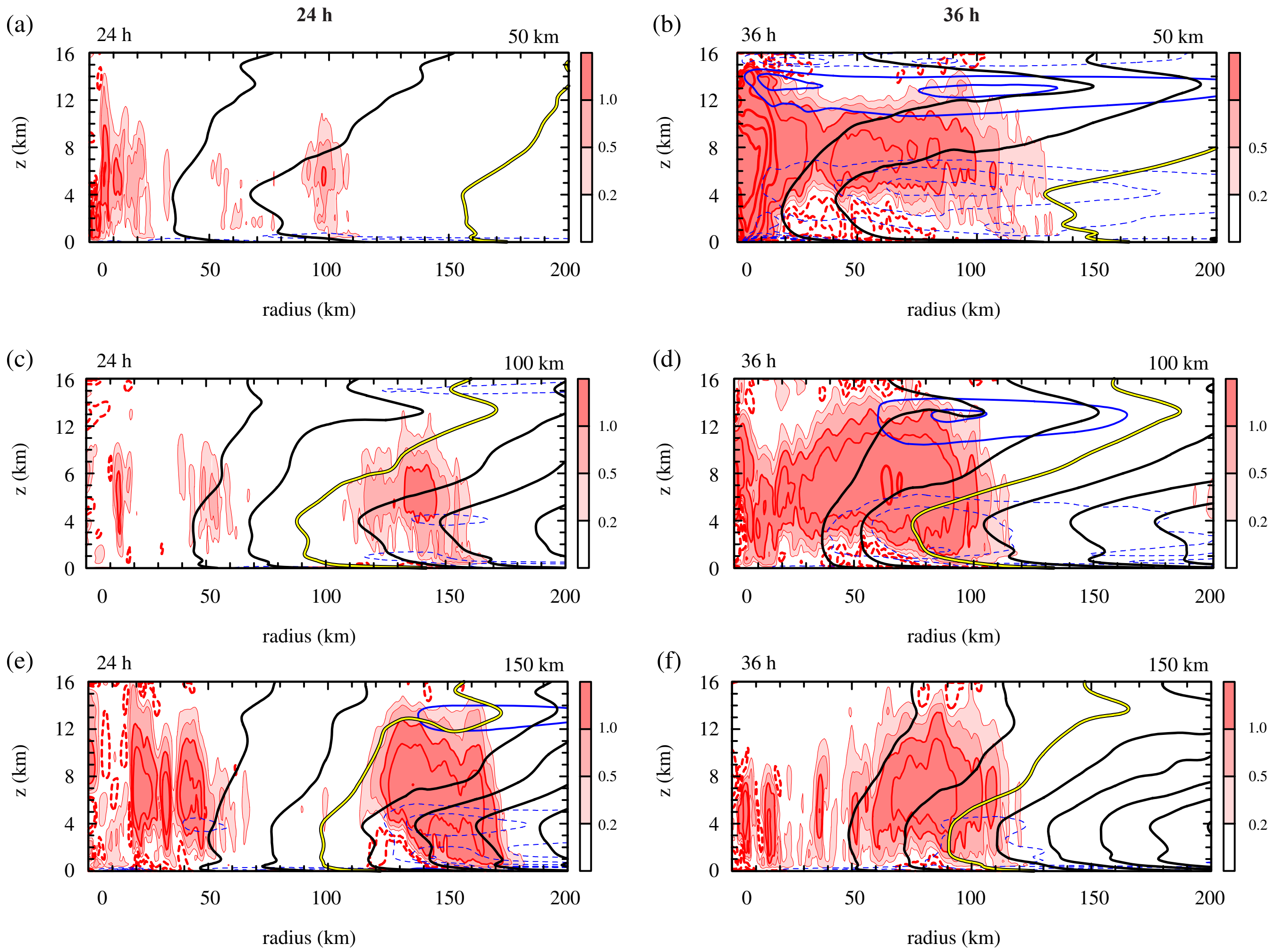

Figure 12. Vertical cross-sections of the azimuthally averaged, 3 h time-averaged radial velocity components centred at (a, c, e) 24 h and (b, d, f) 36 h in (a, b) E1, (c, d) E2 and (e, f) E3. Contour intervals are as follows. Radial velocity: thick blue contours 2 m s^{-1}, dashed negative, thin blue dashed contours every 0.5 m s^{-1} down to -1.5 m s^{-1}. Diabatic heating rate: thin red contours 0.2 and 0.5 K day^{-1}, dashed curves negative values, thick red contours every 1 K day^{-1}. Shading as indicated on the side bar. Absolute angular momentum: thick black contours every 2×10^5 m^2 s^{-1}, with the 6×10^5 m^2 s^{-1} contour highlighted in yellow. [Colour figure can be viewed at wileyonlinelibrary.com].

of 57.5, 80 and 97.5 km), although this increase in moisture is not as large as in E1 and E2 and it takes longer for sustained moistening to occur at the vortex centre (at about 40 h).

To illustrate the inward migration of deep convection further, in Figure 9 we show time–height cross-sections of vertical mass flux averaged over a 20 km × 20 km column, centred on the circulation centre in all three experiments. In E1, there is a burst of deep convection in the column at about 15 h, followed by a convectively suppressed period of about 3 h. Thereafter, from 24 h onwards, there is persistent deep convection in the column. In E2, persistent convection occurs at 30 h, whereas in E3 there is alternating upflow and downflow in the column until about 33 h, when the first strong burst of deep convection occurs. In E3, there are some occurrences of mean downflow in this column until 48 h.

In summary, we have shown that the boundary-layer response is different for initial vortices of different sizes. Namely, the flow exiting the boundary layer is stronger and located closer to the circulation centre as the initial vortex is made smaller. As a result, deep convection near the circulation centre occurs sooner. The larger the initial vortex, the longer it takes for deep convection to focus near the circulation centre.

6. An azimuthally averaged view of vortex evolution

As in our previous studies on tropical cyclogenesis (Kilroy *et al.*, 2017a, 2017b), it proves insightful to examine an azimuthally averaged view of the intrinsically three-dimensional genesis process. To this end, Figures 10 and 11 show vertical cross-sections of 3 h time-averaged tangential velocity, $< v(r,z) >$, and vertical velocity, $< w(r,z) >$, in the three simulations at 24, 36, 48 and 72 h. The time averaging is centred on the time indicated and is based on data output every 15 min.

As early as 24 h, some deep convection occurs near the vortex axis in E1, although at this time there is very little convective activity over the rest of the domain shown (Figure 10(a)). There is some convective activity near a radius of 140 km in E2 at this time, while in E3 deep convection occurs in annuli centred at radii of about 30 and 140 km (Figures 10(c) and (e)). At this time, $V_{\max}$ is essentially the same in all three experiments (Figure 2(a)).

In E1, at 36 h, there is a major change in mean vortex structure, with a large-scale strengthening of tangential winds and a sharp increase in the strength and radial coverage of upward motion (Figure 10(b)). Notably, $V_{\max}$ has migrated to a radius of only 5 km at this time and is located close to the surface, an indication that the boundary-layer spin-up mechanism (Smith *et al.*, 2009; Montgomery and Smith, 2014, 2017) has become operative. At this time, there are regions of very weak downflow (of the order of a few mm s^{-1}) below a height of 4 km centred at a radius of 50 km. This downflow appears to be associated with the evaporation and loading of water vapour, because it coincides with regions of negative diabatic heating rate (described later in Figure 12(b)), but it is a transient feature. Over the next 36 h, the vortex strengthens both within and above the boundary layer. Moreover, by 48 h the tangential flow has become anticyclonic in the upper troposphere, centred at a height of about 13 km (Figure 11(a)).

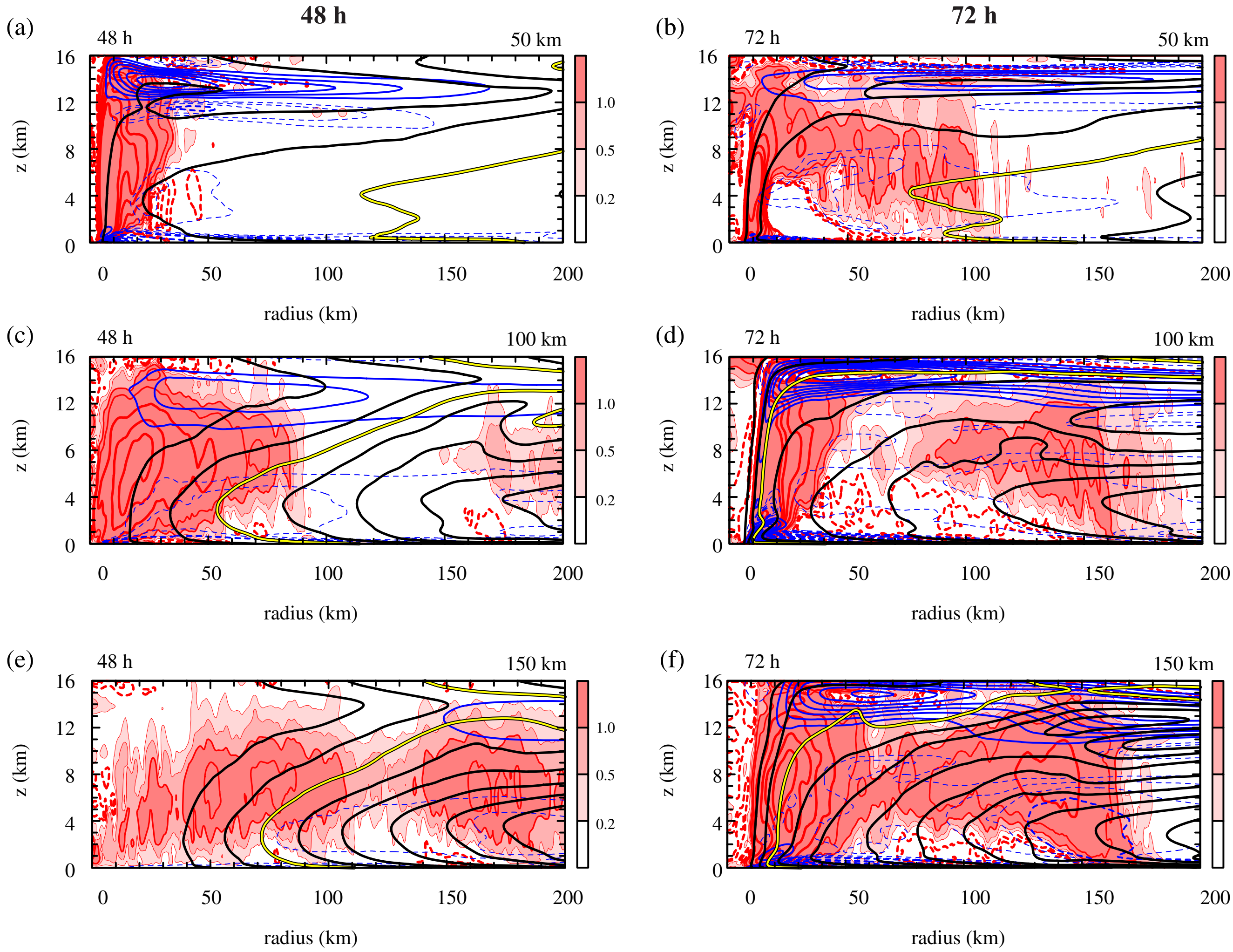

Figure 13. Legend as for Figure 12, but for (a, c, e) 48 h and (b, d, f) 72 h. [Colour figure can be viewed at wileyonlinelibrary.com].

In E2, at 36 h, there are two maxima in the vertical velocity field, one centred on the vortex axis, the other centred at a radius of about 60 km (Figure 10(d)). At this time, $R_{v\max}$ has fallen to a radius of just over 60 km, while the maximum tangential wind has increased only slightly in strength ($V_{\max}$ is less than 8 m s^{-1} at this time). By 48 h, the bulk of the convection has focused closer to the circulation centre and the strongest tangential winds are found near the surface at a radius of just less than 10 km (Figure 11(c)). By this stage, it is apparent that the vortex in E2 is much larger than that in E1, with the 5 m s^{-1} contour extending beyond a radius of 200 km in E2 (the 5 m s^{-1} contour remains inside a radius of 100 km in E1 for the times shown).

In E3, the convection does not focus appreciably inside the radius of maximum winds until after 48 h, although there is a gradual inward migration of $R_{v\max}$ up to this time. At 72 h, there is an eyewall feature of strong vertical velocity (with values $>$ 1 m s^{-1}) centred at a radius of 25 km. As in the other experiments, $V_{\max}$ is located close to the surface (Figure 11(f)).

Figures 12 and 13 compare vertical cross-sections of the azimuthally averaged, 3 h time-averaged radial velocity u, diabatic heating rate $\dot{\theta}$ and absolute angular momentum M at 24, 36, 48 and 72 h in the three simulations. The time averaging is centred on the time indicated and is based on data output every 15 m.

At 24 h (Figure 12, left panels), there is a shallow layer of weak inflow near the surface in E1, not more than about 0.5 m s^{-1} in magnitude, although at this time there is no signal above the boundary layer. Inflow of this magnitude at these radii is consistent with that in the slab boundary-layer calculation in Figure 6(a), but the suction effect of convection might also be playing a role. In E2 and E3, there is some inflow in the low to mid troposphere, presumably associated with the diabatic heating maximum, in each case located at a radius of about 150 km.

At 36 h, (Figure 12, right panels) there is a significant change from 12 h earlier in E1 and E2, but not in E3. In E1, there is broad-scale inflow up to a height of 7 km and out to a radius of 200 km, with the maximum exceeding 1.5 m s^{-1} magnitude, although the strongest inflow (slightly exceeding 5 m s^{-1} in magnitude) occurs near the surface within a radius of 20 km and is presumably a reflection of the strengthened boundary-layer inflow, as the tangential circulation above the boundary layer is already strong at this time (Figure 10(b)). The M-surfaces have migrated further inwards in the region of maximum mid-level inflow, leading to a spin-up of the tangential winds at this height. In E2 at this time, the mid-level inflow and upper outflow do not extend further inward than 40 km radius, while in E3 the radial velocity field is still relatively weak.

At 48 h (Figure 13, left panels), the vortex in E1 has many features of a mature tropical cyclone, including an outflow region located just above the strong near-surface inflow layer. There is still weak inflow in the low to mid troposphere and, as expected, the M-surfaces show a prominent inward-pointing nose at this level. At this time in E2, the near-surface inflow has increased in strength, while the prominent features of the overturning circulation (inflow in the lower troposphere and outflow above) have moved inwards. At this time in E3, the radial velocity field is still relatively weak and the prominent features of the overturning circulation lie beyond a radius of 100 km, although the M-surfaces have moved inwards.

By 72 h (Figure 13, right panels), there is a mature cyclone in all three experiments. In E3, the strongest inflow now occurs near the surface at a radius of about 20 km, although there is still relatively strong ($>$2 m s^{-1}) mid-level inflow centred at a radius of 150 km, stronger indeed than in E2 at that radius. This inflow contributes in spinning up the outer circulation. In E1 at this time, the radial inflow is relatively weak at all heights beyond a radius of 150 km. Of course, the inward radial displacement of the M-surfaces depends on a time integral of the radial flow and not on the instantaneous values, but it is clear that the values of M at large radii are largest in the case of E3 and smallest in the case of E1, indicating that time-mean inflow at large radii increases with the initial vortex size.

Note that, at 72 h, the diabatic heating rate is stronger and covers a broader range of radii as the initial vortex size is increased and the inflow in the low to mid troposphere beyond a radius of 100 km is stronger also. The stronger inflow, in combination with the larger radial gradient of M (i.e. larger inertial stability), leads to a faster spin-up of the tangential winds in the outer part of the vortex. This behaviour is consistent with the findings of Fudeyasu and Wang (2011) referred to in the Introduction and is as one would expect: when deep convection is located at large radii, it will induce inflow on its outer flank, leading to an inward displacement of the M surfaces and thereby a spin-up of the tangential winds above the frictional boundary layer, where M is approximately conserved. If there is little or no outer convection, the inflow at large radii will be weaker and the spin-up there will be correspondingly weaker.

In summary, deep convection focuses near the vortex axis sooner with a smaller initial vortex. Boundary-layer dynamics control where the low-level ascent out of the boundary layer occurs, which is where the CIN is reduced the most. In this way, the boundary layer determines where the first bout of deep convection occurs. As described above, when deep convection develops, the inflow it induces above the boundary layer leads to a strengthening of the tangential winds there and this strengthening occurs earlier when the initial vortex size is reduced. In turn, the strengthening winds above the boundary layer lead to an evolution of the boundary-layer flow and its thermodynamic properties. In this way, there is a tight coupling between the boundary-layer dynamics and thermodynamics and the radial and vertical distribution of the diabatic heating rate (Kilroy *et al.*, 2016). As explained in the previous paragraph, the broader and larger diabatic heating rate that emerges as the size of the initial vortex is increased explains why the outer core vortex size increases also.

7. Conclusions

We have presented three idealized, high-resolution, numerical simulations designed to investigate the effects of initial vortex size on tropical cyclogenesis and intensification. The simulations were carried out starting with weak initial vortices with a maximum tangential wind speed 5 m s^{-1} located at radii of either 50, 100 or 150 km. In each simulation, there is a progressive organization of convectively induced, cyclonic relative vorticity into a monopole structure. This organization takes longer and genesis occurs later when the size of the initial vortex is increased, but the vorticity monopole that develops becomes larger in radius. Consistent with previous studies starting from stronger initial vortices, the larger the initial vortex, the larger the inner and outer core sizes as measured by the radius of maximum tangential wind speed and the radius of gale force winds, respectively. As the size of the initial vortex is increased, so is the lifetime-maximum tangential wind speed.

An explanation for the earlier convective organization and genesis for a small initial vortex is offered in terms of boundary-layer dynamics. A simple slab boundary-layer model shows that, the smaller the initial vortex, the upflow at the top of the boundary layer is stronger and located closer to the circulation centre. Even though the upflow is relatively weak (of the order of a few mm s^{-1}), it is sufficient to provide a location with low convective inhibition, where deep convection can focus and amplify the vertical vorticity locally. The explanation is supported by a comparison of time–radius diagrams of vertical velocity near the top of the boundary layer from the three simulations.

When the initial vortex is larger, the distribution of diabatic heating rate is broader and stronger and leads to stronger inflow at large radii. The stronger inflow, in combination with the larger radial gradient of absolute angular momentum, leads to a more rapid spin-up of the tangential winds in the outer part of the vortex.

The results reported herein serve to underpin a frequently cited observation that, when environmental conditions are favourable, small storms tend to spin up much faster than larger ones. Moreover, while observations do not show a clear relationship between intensity and size, our idealized simulations do suggest that tropical cyclones that develop slowly within a large initial circulation have the capability of becoming stronger than those originating from small initial disturbances. These results may be of interest to forecasters, although we are conscious of the fact that our idealized calculations neglect the effects of vertical wind shear, which may limit their applicability to real-world situations that forecasters have to contend with.

Acknowledgements

The authors acknowledge financial support for tropical cyclone research from the German Research Council (Deutsche Forschungsgemeinschaft) under Grant numbers SM30/23-3 and SM30/23-4 and the Office of Naval Research Global under Grant No. N62909-15-1-N021.

References

Bryan GH, Fritsch JM. 2002. A benchmark simulation for moist nonhydrostatic numerical models. *Mon. Weather Rev.* **130**: 2917–2928.

Bryan GH, Rotunno R. 2009. The maximum intensity of tropical cyclones in axisymmetric numerical model simulations. *Mon. Weather Rev.* **137**: 1770–1789.

Chan K, Chan J. 2012. Size and strength of tropical cyclones as inferred from QuikSCAT data. *Mon. Weather Rev.* **140**: 811–824.

Chan K, Chan J. 2014. Impacts of initial vortex size and planetary vorticity on tropical cyclone size. *Q. J. R. Meteorol. Soc.* **140**: 2235–2248.

Chavas DR, Emanuel KA. 2010. A QuikSCAT climatology of tropical cyclone size. *Geophys. Res. Lett.* **37**: L18816. https://doi.org/10.1029/2010GL044558.

DeMaria M, Pickle JD. 1988. A simplified system of equations for simulation of tropical cyclones. *J. Atmos. Sci.* **45**: 1542–1554.

Dunion JP. 2011. Rewriting the climatology of the tropical North Atlantic and Caribbean Sea atmosphere. *J. Clim.* **24**: 893–908.

Frisius T. 2015. What controls the size of a tropical cyclone? Investigations with an axisymmetric model. *Q. J. R. Meteorol. Soc.* **141**: 2457–2470.

Fudeyasu H, Wang Y. 2011. Balanced contribution to the intensification of a tropical cyclone simulated in TCM4: Outer-core spin-up process. *J. Atmos. Sci.* **68**: 430–449.

Kaplan J, DeMaria M. 2003. Large-scale characteristics of rapidly intensifying tropical cyclones in the North Atlantic basin. *Weather and Forecasting* **18**: 1093–1108.

Kilroy G, Smith RK. 2016. A numerical study of deep convection in tropical cyclones. *Q. J. R. Meteorol. Soc.* **142**: 3138–3151.

Kilroy G, Smith RK, Montgomery MT. 2016. Why do model tropical cyclones grow progressively in size and decay in intensity after reaching maturity? **73**: 487–503.

Kilroy G, Smith RK, Montgomery MT. 2017a. A unified view of tropical cyclogenesis and intensification. *Q. J. R. Meteorol. Soc.* **143**: 450–462.

Kilroy G, Smith RK. 2017b. The role of boundary layer friction on tropical cyclogenesis and intensification. *Q. J. R. Meteorol. Soc.* https://doi.org/10.1002/qj.3104.

Kimball SK, Mulekar MS. 2004. A 15-year climatology of North Atlantic tropical cyclones. Part I: Size parameters. *J. Clim.* **17**: 3555–3575.

Liu KS, Chan JCL. 1999. Size of tropical cyclones as inferred from ERS-1 and ERS-2 data. *Mon. Weather Rev.* **127**: 2992–3001.

Lu X, Yu H, Lei X. 2011. Statistics for size and radial wind profile of tropical cyclones in the western North Pacific. *Acta Meteorol. Sin.* **25**: 104–112.

Merrill RT. 1984. A comparison of large and small tropical cyclones. *Mon. Weather Rev.* **112**: 1408–1418.

Montgomery MT, Smith RK. 2014. Paradigms for tropical-cyclone intensification. *Aust. Meteorol. Oceanogr. J.* **64**: 37–66.

Montgomery MT, Smith RK. 2017. Recent developments in the fluid dynamics of tropical cyclones. *Annu. Rev. Fluid Mech.* **49**: 541–574.

Montgomery MT, Davis C, Dunkerton T, Wang Z, Velden C, Torn R, Majumdar SJ, Zhang F, Smith RK, Bosart L, Bell MM, Haase JS, Heymsfield A, Jensen J, Campos T, Boothe MA. 2012. The Pre-Depression Investigation of Cloud Systems in the Tropics (PREDICT) Experiment: Scientific basis, new analysis tools and some first results. *Bull. Am. Meteorol. Soc.* **93**: 153–172.

Rotunno R, Emanuel KA. 1987. An air–sea interaction theory for tropical cyclones. Part II: Evolutionary study using a nonhydrostatic axisymmetric numerical model. *J. Atmos. Sci.* **44**: 542–561.

Rudeva I, Gulev SK. 2007. Climatology of cyclone size characteristics and their changes during the cyclone life cycle. *Mon. Weather Rev.* **135**: 2568–2587.

Smith RK. 2006. Accurate determination of a balanced axisymmetric vortex. *Tellus* **58A**: 98–103.

Smith RK. 2012. Observations of the convective environment in developing and non-developing tropical disturbances. *Q. J. R. Meteorol. Soc.* **138**: 1721–1739.

Smith RK, Montgomery MT. 2015. Towards clarity on understanding tropical cyclone intensification. *J. Atmos. Sci.* **72**: 3020–3031.

Smith RK, Montgomery MT, Nguyen SV. 2009. Tropical-cyclone spin up revisited. *Q. J. R. Meteorol. Soc.* **135**: 1321–1335.

Smith RK, Montgomery MT, Schmidt C. 2011. Dynamical constraints on the intensity and size of tropical cyclones. *Q. J. R. Meteorol. Soc.* **137**: 1841–1855.

Smith RK, Kilroy G, Montgomery MT. 2015. Why do model tropical cyclones intensify more rapidly at low latitudes? *J. Atmos. Sci.* **72**: 1783–1804.

Tsuji H, Itoh H, Nakajima K. 2016. Mechanism governing the size change of tropical cyclone-like vortices. *J. Meteorol. Soc. Jpn.* **94**: 219–236.

Weatherford CL, Gray WM. 1988. Typhoon structure as revealed by aircraft reconnaissance. Part I. Data analysis and climatology. *Mon. Weather Rev.* **116**: 1032–1043.

Wissmeier U, Smith RK. 2011. Tropical-cyclone convection: The effects of ambient vertical vorticity. *Q. J. R. Meteorol. Soc.* **137**: 845–857.

Xu J, Wang Y. 2010. Sensitivity of the simulated tropical cyclone inner-core size to the initial vortex size. *Mon. Weather Rev.* **138**: 4135–4157.

Yuan JD, Wang D, Wan Q, Liu C. 2007. A 28-year climatological analysis of size parameters for northwestern Pacific tropical cyclones. *Adv. Atmos. Sci.* **24**: 24–34.

